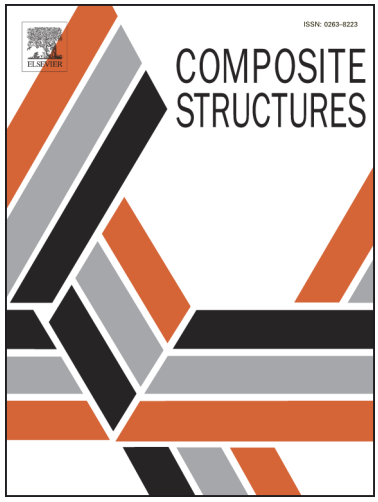

Piezoelectric energy harvester composite under dynamic bending with implementation to aircraft wingbox structure

M. Akbar, J.L. Curiel-Sosa

PII: S0263-8223(16)30734-6
DOI: http://dx.doi.org/10.1016/j.compstruct.2016.06.010
Reference: COST 7532

To appear in: *Composite Structures*

Please cite this article as: Akbar, M., Curiel-Sosa, J.L., Piezoelectric energy harvester composite under dynamic bending with implementation to aircraft wingbox structure, *Composite Structures* (2016), doi: http://dx.doi.org/10.1016/j.compstruct.2016.06.010

Piezoelectric energy harvester composite under dynamic bending with implementation to aircraft wingbox structure

M. Akbar*, J.L. Curiel-Sosa

Department of Mechanical Engineering, The University of Sheffield, Sir Frederick Mappin Building, Mappin Street, S1 3JD Sheffield, United Kingdom

Abstract

In this paper, an investigation on the energy harvesting exerted by the dynamic bending responses of a piezoelectric embedded wingbox is presented. An innovative hybrid mathematical/computational scheme is built to evaluate the energy harvested by a mechanical system. The governing voltage differential equations of the piezoelectric composite beam are coupled with the finite element method output. The scheme is able of evaluating various excitation forms including dynamic force and base excitation. Thus, it provides the capability to analyse a complicated structure with a more realistic loading scenario. Application to the simulation of a notional jet aircraft wingbox with a piezoelectric skin layer is shown in some detail. The results pointed out that the electrical power generated can be as much as 25.24 kW for a 14.5 m wingspan. The capabilities and robustness of the scheme are shown by comparison with results from the literature.

Keywords: Piezoelectric, Energy Harvester, Dynamic Bending, Aircraft Wingbox

1. Introduction

In the past decade, the interest on the multifunctional structure application has grown in a significant manner. The multifunctional structures, aside of load bearing capability, possess multiple functionality included non-structural function [1, 2]. The structural power material system [1], so called the energy storing/harvesting structure [2], is targeted in the work presented in this paper.

Numerous energy harvesting related articles limited to the small-scale structures have been published in the last few years. Thus, several review articles [3, 4, 5] presented the resulting range of power from the order of microwatts to tens of watts. Along with the increase of researches in this area, comes an interest to implement harvesting capability in the larger structures, i.e. bridges, aircraft structures. As an attempt to address this interest, a novel approach to evaluate the potential energy harvesting of a civil jet aircraft structure is presented.

For the small-scale aerial vehicle, one of the successful implementation of energy storing/harvesting structure is seen on The Wasp UAV [6, 7]. The weight of conventional battery package is eliminated and the flight endurance is enhanced through the structural-battery laminated wing skin. However, this structural-battery is only rechargeable while the aircraft is in the ground and it is not applicable for harvesting energy in the operational flight.

Anton and Inman [8] presented a remote control aircraft is embedded with solar panels and piezoelectric patches for a study of energy harvesting during flight operation. It was found that the energy harvesting systems were able to support the main electrical power sources of the aircraft (piezoelectric pacthes charged up to 70% capacity of 4.6 mJ internal capacitor). In line with this study, the design and experimental test of a self-charging wing spar for UAV were performed by [9, 10]. The self-charging wing spar comprised of piezoelectric layers to harvest the energy generated via base excitation vibration and thin-film batteries as the energy storage.

The methodology to design the energy harvesting wing spar [9] was based on the mathematical model of a cantilevered piezoelectric energy harvester under

*Corresponding author

Email addresses: makbar2@sheffield.ac.uk (M. Akbar), j.curiel-sosa@sheffield.ac.uk (J.L. Curiel-Sosa)

URL: http://www.jlcurielsosa.org (J.L. Curiel-Sosa)

base excitation proposed by Erturk and Inman [11]. The dynamic responses of the cantilevered beam due to base excitation loading, i.e. the cantilever root undergoes transverse dynamic motions causing the beam structures vibrate along the span, are coupled with the electromechanical constitutive equations of the piezoelectric materials to evaluate the harvested energy. This mathematical model was able to estimate the voltage and power frequency responses function of a notional cantilever beam around the first three bending modes.

Prior to the Erturk-Inman model [11], several mathematical modelling issues of piezoelectric energy harvesters were addressed by [12]. The reverse piezoelectric coupling in the mechanical equation was investigated. Based on [12], the absence of the reverse piezoelectric coupling from several literature lead to some incorrect results. The model was validated afterwards againts the experimental results by [13]. The inclusion of reverse piezoelectric effect on the mathematical model yields good comparisons with experimental results.

Furthermore, the mathematical model of cantilevered piezoelectric energy harvester under base excitation has been evolving since. Thus, the piezoelectric energy harvesters with two degree of freedoms airfoil [14] and planar lifting surface [15] under aeroelastic vibration, i.e. flutter instability case, were developed. In addition to the time domain model with unsteady aerodynamic calculation via Vortex Lattice Method proposed by [15], a frequency domain model with unsteady aerodynamic calculation via Doublet Lattice Method has been formulated by [16]. A coupled model considering the electromagnetic field is proposed by [17]. In addition, [18] developed a three degree of freedoms model for an airfoil actioned by control surfaces. These models [14, 15, 16, 17, 18] were able to predict the voltage and power responses at the flutter speed with the combination of unsteady aerodynamic loads. The airfoil model [14] was also validated against the wind tunnel test results.

Recently, Amini et al. [19, 20] built a finite element model for energy harvesters made of the functionally graded piezoelectric materials (FGPMs). The FGPMs were implemented in order to enhance the mechanical performance of the piezoelectric composites by avoiding stress concentration and crack propagation.

The interested reader is referred to a comprehensive review article by Abdelkefi [21] which discusses numerous aeroelastic energy harvesting papers published within the period 2000′s - 2015. Topics on flutter of airfoil, vortex induced vibration (VIV) of cylinders and galloping were reviewed. Most of the proposed mathematical models were developed for flutter-based energy harvesters of small-scale power generation application (maximum in order of tens of miliwatts). Abdelkefi stated that only Xiang et al. [22] reported the study on harvesting performance of piezoelectric wing under discrete gust load based on a mathematical model.

Flutter is unlikely to be encountered during normal flight of civil jet aircraft and the structure constructed from more complicated configuration, i.e. skins, ribs and spars. Therefore, to address some of the issues of previous works, a novel hybrid mathematical/computational scheme to evaluate energy harvesting is proposed herein. A piezoelectric composite beam model under dynamic bending load is considered. The beam represents the aircraft wing and the bending load represents the cruise and/or gust load. The governing voltage differential equations of the beam is coupled with a finite element method output, so that a non uniform cross section structure is evaluable. The scheme is presented in the following sections of this paper, as well as an application to the simulation of a notional civil jet aircraft wingbox with piezoelectric layer.

2. Mathematical Model

In this section, the mathematical model for the energy harvesting of a piezoelectric cantilever beam under dynamic bending load is presented. The description of the electrical and mechanical characteristics of the isotropic material are shown in figures 1 and 2.

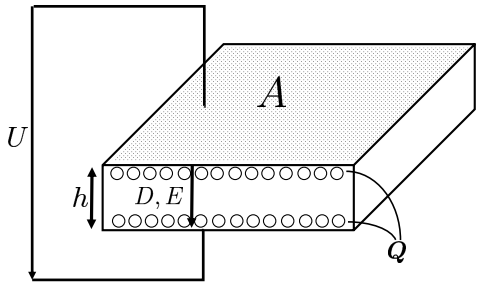

Figure 1: Specimen loaded by voltage, U

Figure 1 shows the electrical charges , Q (depicted by circles 'o'), accumulated in a specimen due to voltage load, U. The permittivity of material, ε, allows

generation of the electrical displacement, D. Thus, creating an electrical field, E [23].

$$D = \frac{Q}{A} \tag{1}$$

$$Q = CU \tag{2}$$

$$C = \varepsilon \frac{A}{h} \tag{3}$$

$$D = \varepsilon E \tag{4}$$

where Q, C, U, D, and E are the electrical charges (Coulomb), capacitance (Farad), voltage (Volt), electrical displacement (Coulomb/m^2) and electrical field (Volt/m); A and h are the surface area (m^2) and thickness (m) of the specimen. ε, is the permittivity at a constant stress field (Farad/m), where

$$\varepsilon = \varepsilon_r \varepsilon_0 \tag{5}$$

ε_0 is the vacuum permittivity (8.85x10^{-12} Farad/m) and ε_r is the relative permittivity. In other cases, it is also common to express equation (4) with the permittivity at a constant strain field [24].

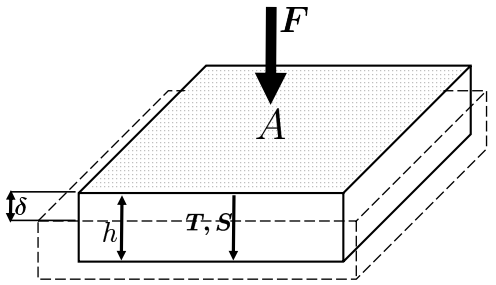

Figure 2: Specimen loaded by force, F

Figure 2 shows a specimen made of an isotropic material loaded by a force, F. A deformation, δ (reducing the thickness) is exerted by the force, F. Thus, the mechanical strain, S and stress, T, are generated [23]. In a homogeneous, isotropic material, and linear-elastic region, relationship of those mechanical quantities are

$$T = \frac{F}{A} \tag{6}$$

$$S = \frac{\delta}{h} \tag{7}$$

$$S = sT \tag{8}$$

For piezoelectric materials, coupled between mechanical and electrical domain is considered. A piezoelectric charge constant, d, denotes how much an electrical load, i.e. voltage, affect the mechanical deformation and vice versa [23]. According to the IEEE Standard on Piezoelectricity [24], the constitutive equations (4) and (8) could be written as a set of coupled electromechanical equations.

$$D = \varepsilon E + dT \tag{9}$$

$$S = dE + sT \tag{10}$$

Ballas [25, 26] derived the mathematical models of piezoelectric beam bending actuator under static and dynamic bending loads. A composite beam made of two parts, the substrate layers (non-piezoelectric material) and the electrically active layers (piezoelectric material) is shown in Figure 3.

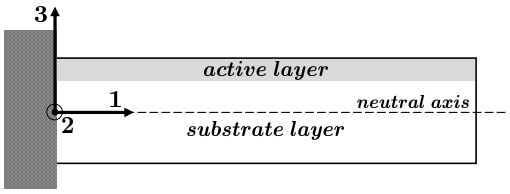

Figure 3: A cantilevered multilayer beam with piezoelectric layer

Ballas [26] assumes that:

1) The electrical field only generated in z-direction $E1 = E2 = 0$ & $E3 \neq 0$;

2) Only one mechanical stress components generated in the x-direction $T2 = ...T6 = 0$ & $T1 \neq 0$;

3) All active layers are driven by the same voltage along z-direction, $U3$.

Therefore, equations (9) and (10) become

$$D_3 = \varepsilon_{33} E_3 + d_{31} T_1 \tag{11}$$

$$S_1 = d_{31} E_3 + s_{11} T_1 \tag{12}$$

Figure 4 shows a bending moment, M, is applied to a cantilever beam. Transverse displacement, ζ, and bending slope, θ, are created. At an arbitrary point,P, located at a distance, z, from the neutral axis, strain is generated.

The mechanical strain at x-direction is expressed as

$$S_1 = -z \frac{\partial^2 \zeta}{\partial x^2} \tag{13}$$

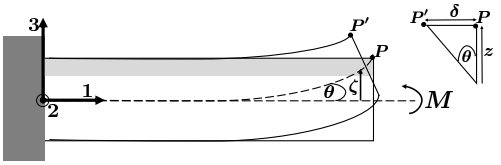

Figure 4: A cantilever beam loaded by bending moment, M

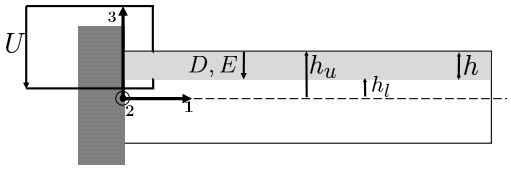

Figure 5: A cantilever beam with piezoelectric layer loaded by voltage, U

In the active layer, the electrical voltage, U, generated an electrical field, E, such as shown in Figure 5.

$$U = \int_{h_l}^{h_u} E_3 dz \tag{14}$$

Incorporating equations (13) and (14) into equations (11) and (12), yields

$$D_3 = \frac{U}{h}\left(\varepsilon_{33} - \frac{d_{31}^2}{s_{11}}\right) - \frac{d_{31}(h_u^2 - h_l^2)}{2s_{11}h}\frac{\partial^2\zeta}{\partial x^2} \tag{15}$$

Furthermore, the electrical charges at a certain point, Q, is determined by applying Gausss theorem over an area, A, as

$$Q = \oint D.dA \tag{16}$$

Consider a uniform cross section shown in Figure 6. $Q(x)$, the electrical charges from the root until a certain point at length x, could be expressed as

$$Q(x) = \frac{U(x)bx}{h}\left(\varepsilon_{33} - \frac{d_{31}^2}{s_{11}}\right) - \frac{d_{31}(h_u^2 - h_l^2)b}{2s_{11}h}\frac{\partial\zeta(x)}{\partial x} \tag{17}$$

Defines

$$\Gamma_1 = \frac{bx}{h}\left(\varepsilon_{33} - \frac{d_{31}^2}{s_{11}}\right) \tag{18}$$

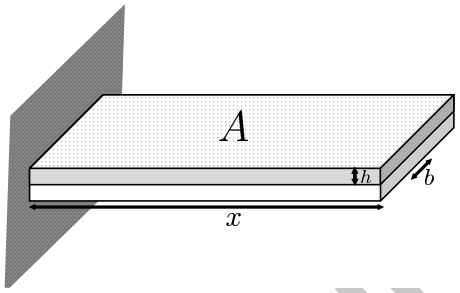

Figure 6: A cantilever beam with uniform cross-section

and,

$$\Gamma_2 = \frac{d_{31}(h_u^2 - h_l^2)b}{2s_{11}h} \tag{19}$$

For a time-dependant motion, equation (17) becomes

$$Q(x,t) = \Gamma_1(x)U(x,t) - \Gamma_2(x)\frac{\partial\zeta(x,t)}{\partial x} \tag{20}$$

Γ_2 denotes an internal bending moment, M_{piezo}, which is exerted by a unit of voltage, U [26].

$$M_{piezo} = \Gamma_2 U \tag{21}$$

The concept of M_{piezo} was used by Ballas [26] to evaluate the static deformation of a piezoelectric beam actuator driven by a voltage, U. This concept resulted in a good comparison with experimental results [27].

For the energy harvesting purpose, equation (20) is further elaborated. An electrical circuit connected to the piezoelectric beam is considered.

$$\frac{\mathrm{d}Q(x,t)}{\mathrm{d}t} = I(x,t) = \frac{U(x,t)}{R} \tag{22}$$

where, I is the electrical current (Ampere) and R is the resistance load (Ohm, Ω).

Insertion of equation (20) to (22), yields a differential equation in terms of U,

$$\Gamma_1\frac{\mathrm{d}U(x,t)}{\mathrm{d}t} - \Gamma_2\frac{\mathrm{d}}{\mathrm{d}t}\left(\frac{\partial\zeta(x,t)}{\partial x}\right) = \frac{U(x,t)}{R} \tag{23}$$

Assumes a harmonic oscillation motion

$$\zeta(x,t) = Z(x)e^{i\omega t} \tag{24}$$

$$U(x,t) = \bar{U}(x)e^{i\omega t} \tag{25}$$

where Z is the transverse displacement amplitude (meter) and $\bar{U}$ is the voltage amplitude.

Equation (23) becomes

$$i\omega\Gamma_1\bar{U} - i\omega\Gamma_2\frac{\partial Z(x)}{\partial x} = \frac{\bar{U}}{R} \tag{26}$$

The displacement, $Z(x)$, is comprised of the displacement due to mechanical load, Z_{mech}, and accumulated electrical load, Z_{elec}. This Z_{elec} is generated by the internal forces due to the reverse piezoelectric effect. Thus,

$$\frac{\partial Z}{\partial x} = \frac{\partial Z_{mech}}{\partial x} + \frac{\partial Z_{elec}}{\partial x} \tag{27}$$

Applying the concept of M_{piezo}, the bending slope due to electrical load is

$$\frac{\partial Z_{elec}}{\partial x} = H_{\alpha m} M_{piezo} \tag{28}$$

or,

$$\frac{\partial Z_{elec}}{\partial x} = H_{\alpha m}\Gamma_2 U \tag{29}$$

$H_{\alpha m}$ is the admittance function (rad/Newton-meter) of the displacement slope (angle) due to an applied unit of moment at the tip. This admittance function could be obtained analytically [25] or computationally.

The reverse piezoelectric effects as explained through equations (27) to (29) has been investigated by numerous researchers. Erturk and Inman [28], cited the work of Lu, et al. [29] and Beeby, et al. [30], stated that without the reverse effect the responses were highly inaccurate and overestimated the experimental results.

However, as far as authors knowledge, the concept of M_{piezo} had only been used for the actuator case. Hence, for energy harvesting purpose it is a novel concept to evaluate the reverse piezoelectric effect.

Incorporating equations (27) and (29), then equation (26) becomes

$$\bar{U}(x) = \frac{i\omega\Gamma_2(x)\frac{\partial Z_{mech}(x)}{\partial x}}{-\frac{1}{R} + i\omega\Gamma_1(x) - i\omega\Gamma_2(x)^2 H_{\alpha m}(x)} \tag{30}$$

At the tip of the beam (x = L), the voltage amplitude is calculated by

$$\bar{U}(L) = \frac{i\omega\Gamma_2(L)\frac{\partial Z_{mech}(L)}{\partial x}}{-\frac{1}{R} + i\omega\Gamma_1(L) - i\omega\Gamma_2(L)^2 H_{\alpha m}(L)} \tag{31}$$

From equation (31), the maximum electrical power generated, P_{max} (Watt), could be expressed as

$$P_{max} = \frac{\bar{U}^2}{R} \tag{32}$$

3. Code Algorithm

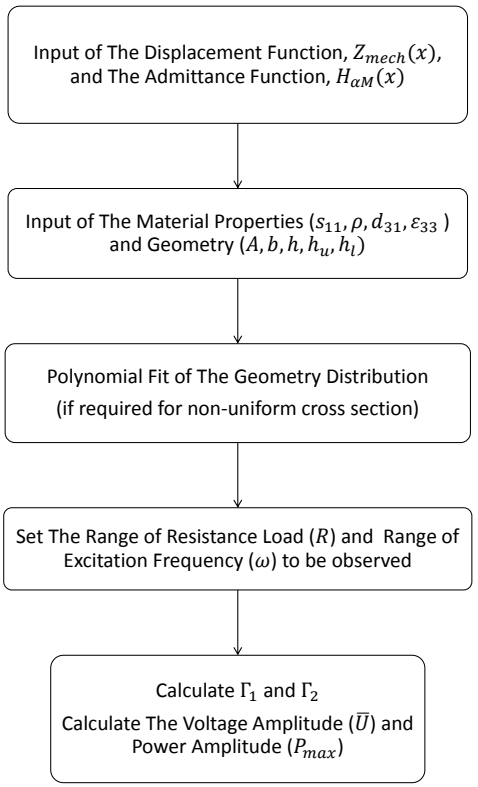

Figure 7: Schematic diagram of the energy harvesting system evaluation process

A computational code to evaluate the harvested energy based on equations (31) and (32) is built using MATLAB©. The process flow of the present code is shown in Figure 7. However, equation (31) is derived based on a uniform cross-section beam. Therefore, an approximation, i.e. polynomial function, is used to accommodate the geometrical distribution along the cantilever span ($hu(x)$, $hl(x)$, $b(x)$).

Aside of the geometries and material properties, two key inputs of the present code are

1) the displacement slope (bending angle) function due to mechanical loading, $\frac{\partial Z_{mech}}{\partial x}$, and

2) the admittance function of bending angle due to a unit of moment, $H_{\alpha m}$.

Both of the inputs could be obtained via analytical solutions or computational method, i.e. finite element method (FEM). In a computational simulation, $H_{\alpha m}$, is obtained by applying 1 unit (i.e 1

Nm) of moment at the neutral axis of the beams tip. Hence, a hybrid mathematical/computational simulation could be performed via the present code. As the results, voltage and power amplitude are calculated for a range of excitation frequency, ω and a range of external resistance load ,R.

4. Validation

In this section, validation for the mathematical model and computational procedure of the previous sections is presented. The results of Erturk and Inman [31, 32] for the bimorph cantilevered energy harvesters under base excitation are used as benchmarks.

Table 1: Bimorph piezoelectric energy harvester properties [31]

Properties	Piezo - ceramics	Sub - structure
Length, L (mm)	30	30
Width, b (mm)	5	5
Thickness, h (mm)	0.15(each)	0.05
Material	PZT-5A	Aluminium
Density, ρ (kg/m^3)	7750	2700
Elastic modulus, $1/S_{11}$ (GPa)	61	70
Piezoelectric constant, d_{31} (pm/V)	-171	-
Permittivity, ε_{33} (nF/m)	15.045	-

Table 2: Bimorph piezoelectric energy harvester properties [32]

Properties	Piezo - ceramics	Sub - structure
Length, L (mm)	24.53	24.53
Width, b (mm)	6.4	6.4
Thickness, h (mm)	0.265(each)	0.140
Material	PZT-5H	Brass
Density, ρ (kg/m^3)	7500	9000
Elastic modulus, $1/S_{11}$ (GPa)	60.6	105
Piezoelectric constant, d_{31} (pm/V)	-274	-
Permittivity, ε_{33} (nF/m)	30.09	-

Both of the structural dynamic responses based on the analytical solution and FEM simulation are carried on as inputs to evaluate the harvested energy.

Table 3: Natural frequency comparison, configuration from Table 1

	Natural frequency (Hz)		
Mode Shape	Erturk - Inman [31]	Analytical - Present	Finite Element
1^{st} Bending	185.1	185.1	187
2^{nd} Bending	1159.8	1160.1	1162.3
3^{rd} Bending	3247.6	3248.3	3238.5

Table 4: Relative tip displacement comparison, configuration from Table 1

	Relative tip displacement (μm)		
Frequency ratio	Erturk - Inman [31]	Analytical - Present	Finite Element
0.8	-	2.8	2.8
0.9	-	7.4	7.4
1.0	78.0	78.3	155

Erturk-Inman model used the analytical approaches for both structural dynamic analysis and energy harvesting evaluation [31]. Table 3 shows comparison of the natural frequencies for both the analytical solution of and FEM results are in a good agreement with Erturk-Inman′s results [31]. Meanwhile, Table 4 shows the comparison of the relative tip displacements due to 1 μm base excitation amplitude. The excitation frequencies observed are around the 1^{st} bending natural frequency. The comparisons are made based on the ratio of excitation frequency to the 1^{st} bending natural frequency, i.e. frequency ratio 0.8 means 150 Hz for the FEM model and 148.1 Hz for the analytical model.

At the frequency ratios 0.8 and 0.9, the FEM results are in a good agreement with analytical results. However, at the resonance frequency, the displacement of FEM model suddenly increases to almost double of the analytical results. It shows that the FEM model required careful attention to obtain great accuracy at the resonance frequency.

For comparison purpose, a separate code via MATLAB© is built to reconstruct Erturk and Inman′s electromechanical model for a bimorph cantilevered piezoelectric energy harvester under base excitation [31]. Using the configuration from 1, the harvested energy at the short circuit condition with series connection is evaluated.

Figure 8 until Figure 11 show the voltage and amplitudes of the 3 different procedures. Denoted by "Present Model (Analytical)" is the result of the

Table 5: Electrical parameters comparison, configuration from Table 1

	Frequency ratio = 0.8			Frequency ratio = 0.9		
Electrical parameters	Erturk-Inman[31]	Present Model (FEM)		Erturk-Inman[31]	Present Model (FEM)	
Max Voltage(V)	0.0815	0.0816	Δ=0.1%	0.1855	0.1863	Δ=0.4%
Max Power(μW)	0.0253	0.0251	Δ=0.8%	0.1677	0.1707	Δ=1.8%
R at Max Power(kΩ)	265.09	262.85	Δ=0.9%	205.31	201.08	Δ=2.1%

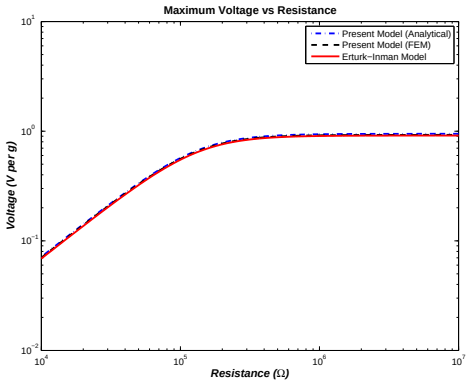

Figure 8: Voltage amplitude vs resistance at 0.8 frequency ratio, configuration from Table 1

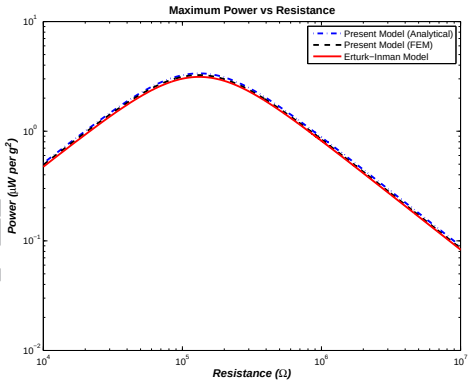

Figure 9: Power amplitude vs resistance at 0.8 frequency ratio, configuration from Table 1

present mathematical model combined with the analytical structural dynamic solutions. Meanwhile, the result via coupling with the FEM model is denoted by "Present Model (FEM)".

The figures are in logarithmic to logarithmic scale, where both the voltage and power are normalized per unit of g (9.81 m/s^2) and g^2, following the way it is presented in [31]. Value of "V per g" is obtained from the voltage amplitude divided by the base acceleration ratio to g, i.e. base amplitude 1 μm and 150 Hz excitation equal with 0.89 m/s^2 base acceleration or 0.09 acceleration ratio. Meanwhile, the electrical power is normalized per unit g^2, or power divided by the square of the acceleration ratio.

Figure 8 until Figure 11 show that the voltage and power amplitude for the 3 procedures are almost coincide, therefore it is difficult to distinguish. In a smaller range of resistance load, it can be seen that the present model results are slightly overestimate the Erturk-Inman model as shown in figures 10 and 11. Detailed comparison for the maximum voltage and power amplitude are given in Table 5. The variances (Δ) to the Erturk-Inman model is increasing as the frequency ratio is closer to resonance frequency. However, it can be seen that the variances are insignificant (less than 5%).

In addition, at the resonance frequency (frequency ratio = 1), the comparisons between present mathematical model incorporating analytical structural dynamic solutions and Erturk-Inman model with different configurations are shown in Table 6. The comparisons shows that the variances are most likely negligible.

5. Wingbox FEM analysis

A test case for a notional civil jet aircraft wingbox is simulated in the present work. The structural dynamic response is carried on via FEM. A common practical case in the operational flight is considered. The dynamic excitation forces is equal with the cruise load. The excitation frequencies observed are around the 1st bending mode natural frequency.

An aircraft wingbox model [33] is taken as the reference for the present simulation. However due to some details of the wingbox are not given, the geometry is simplified based on the available data.

Table 6: Electrical parameters comparison, configuration from Table 1 and Table 2

	Frequency ratio = 1			Frequency ratio = 1		
Electrical parameters	Erturk-Inman[31]	Present Model (FEM)		Erturk-Inman[32]	Present Model (FEM)	
Max Voltage(V)	0.7821	0.7821	Δ=0.0%	2.6078	2.6078	Δ=0.0%
Max Power(μW)	4.3536	4.3538	Δ=0.0%	224.89	224.90	Δ=0.0%
R at Max Power (kΩ)	140.48	140.49	Δ=0.0%	30.239	30.239	Δ=0.0%

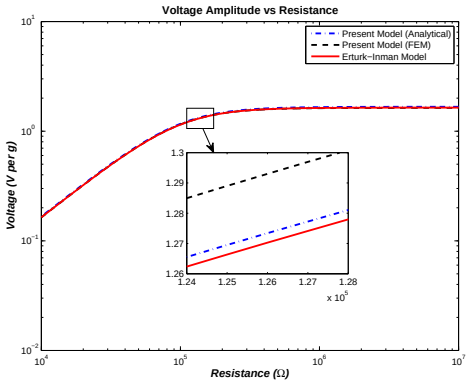

Figure 10: Voltage amplitude vs resistance at 0.9 frequency ratio, configuration from Table 1

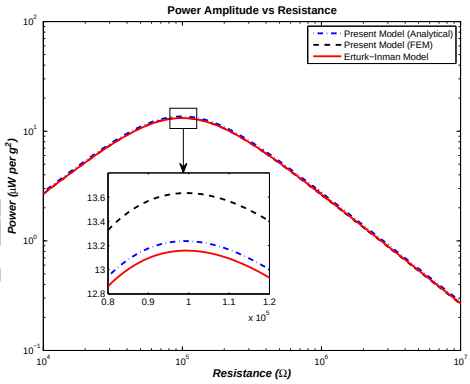

Figure 11: Power amplitude vs resistance at 0.9 frequency ratio, configuration from Table 1

Figure 12 shows the wingbox vertical stiffness distribution. Due to the detail of the ribs cross section is not available from [33], it is assumed that the ribs are plates with rectangular cross section. Figure 13 shows the wingbox layout from topside view. The available data from [33] are the span length of the spar (570 in or 14.48 m), the distance between the front spar and the rear spar at the wing root (90 in or 2.29 m) and at the wing tip (35 in or 0.88 m). For simplification, the front spar length is assumed perpendicular to the ribs at the root and tip. The rear spar is assumed to be straight connecting the trailing edge of the root and tip ribs. The ribs spacing are assumed uniform. Hence, there are 20 ribs with 30 inches spacing in the simplified model.

Other simplifications made for the present simulation are

1) The skins, ribs and spars are assumed as rectangular plates with uniform thickness. The thickness for the skins is 0.24 inches and for the ribs and the spars is 0.29 inches. These are maximum thickness values of the original model[33].

2) The stringers and spar caps are not modelled for the present simulation.

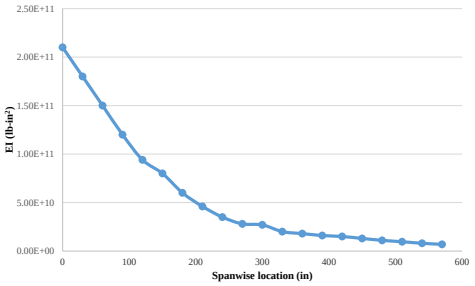

Figure 12: Wingbox vertical stiffness distribution [33]

3) The skins, ribs and spars are made of uniform plates with isotropic material, Al-2219. Later on, for energy harvesting purpose, the upper skin material is replaced by a piezoceramic material, M1832 [27].

Figure 14 shows the wingbox model used for the finite element analysis. The skins, ribs and spars are modelled as quadrilateral shell elements with the thickness as mentioned earlier. The solver used for the simulation is based on the explicit FEM [34, 35]. The translations and rotations (for 3 directions) are fixed at the root and free at the tip. The different material configurations used for the simulation are

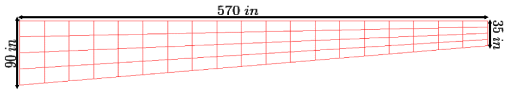

Figure 13: Wingbox topside view layout

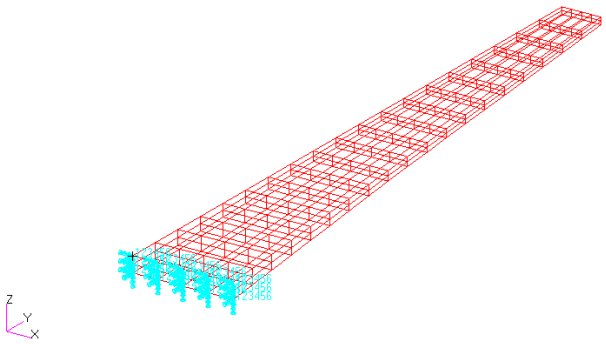

Figure 14: Wingbox model for finite element analysis

1) All of the skins, ribs and spars are modelled by Al-2219 with modulus of elasticity 73.1 GPa (10.6^6 lb-in^2), poissons ratio 0.33 and density 2840 kg/m^3(0.1 lb/in^3). To be called model A, hereafter.

2) The upper skin replaced with piezoceramic material, M1832 with modulus of elasticity 70.7 GPa ($10.3\text{x}10^6$ lb-in^2), poissons ratio 0.33 and density 8100 kg/m^3(0.3 lb/in^3). The piezoceramic M1832 is considered due to its modulus of elasticity is close to common aluminium alloy materials (around 70 GPa). Therefore, the stiffness distribution is not altered significantly. To be called model B, hereafter.

The data given [33], shows that the original model is weighted 2742.5 lbs and the maximum tip displacement is around 30 inches during the ultimate load (2.5 g up gust and 50,000 lbs thrust load). The weight of the aircraft itself is 170,000 lbs and the 2.5 g up gust is equal with 425,000 lbs.

The comparison of the original model [33] and model A is shown in Table 7.

Furthermore, modal analysis is conducted for model A and model B. The natural frequencies comparison between model A and B is shown in Table 8. The modification in model B resulted in a lower

Table 7: Weight and tip displacement, Z_{tip}, original model [33] vs model A

	Weight (lbs)	Z_{tip} - ultimate (in)	Z_{tip} - cruise (in)
Original model	2472.5	30	-
Model A	2415	33.8	13.5

natural frequency than model A for the same mode shape. As the total weight of model B is 4100 lbs and model A is 2415 lbs, the square root of the mass ratio between model A and B is found to be 1.30. This mass ratio is close to the frequency ratio (f_A/f_B) for the first 3 bending modes shapes shown in Table 8.

Table 8: Natural frequency comparison, model A vs model B

	Natural frequency (Hz)		
Mode Shape	Model A	Model B	f_A/f_B
1^{st} Bending	2.16	1.63	1.32
2^{nd} Bending	9.01	6.82	1.32
3^{rd} Bending	21.70	16.46	1.32

Moreover, for the energy harvesting purpose, Model B is analyzed by applying the frequency-dependant forced excitation via a FEM module [36]. The force amplitude is equal with the cruise lift, half of the aircraft weight (85,000 lbs). The excitation frequencies varied from 1, 2 to 3 Hz. These range of frequencies is close to the natural frequency of the 1^{st} mode shape.

6. Wingbox energy harvesting simulation

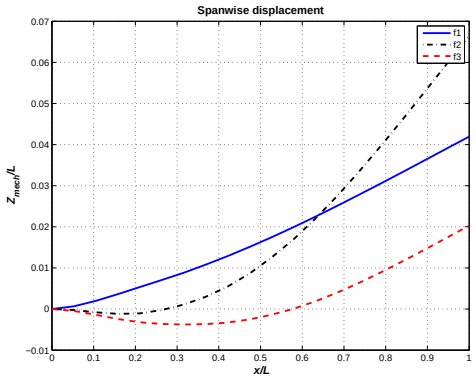

Figure 15: Wingbox dynamic response amplitude along the span

Figure 15 shows the plot of model B displacement functions obtained via the FEM simulation. The plot

shows the non-dimensionalized amplitude, Z_{mech}/L, with respect to the neutral axis. The excitation frequencies observed, f1, f2 and f3, are 1, 2 and 3 Hz. At 1 Hz, the displacement response is mostly influenced by the 1^{st} bending modes, while at 2 Hz and 3 Hz the displacement responses start to be influenced by the 2^{nd} bending modes. At 2 Hz, the tip displacement slope (bending angle) is the highest amongst the other two frequencies, as it is the nearest to 1^{st} resonance frequency (1.63 Hz). Meanwhile, the bending slopes at 1 Hz and 3 Hz are almost parallel from mid-span to the tip.

The voltage amplitude responses are shown in Figure 16. It can be seen that the voltage amplitudes resembled the behaviour of the structural dynamic responses. At 2 Hz, the voltage amplitude is the largest amongst the other two frequencies. While the voltage amplitude at 3 Hz is slightly over the responses at 1 Hz. The voltage responses in Figure 16 also exhibit the similar behaviour with the results displayed in Figure 8 and Figure 10. The voltage responses at first are increasing with the resistance load until at a certain point it undergo an asymptotic behaviour. Hence, from this point, further increment of the resistance load is no more affecting the voltage responses.

Meanwhile, the power amplitude responses are shown in Figure 17. The responses are align with those of the voltage responses. The power amplitude at 2 Hz is the largest amongst the other two frequencies. While the power amplitude at 3 Hz only slightly over the response at 1 Hz. The power responses in Figure 17 also exhibit similar behaviour with those previously shown for the base excitation model in Figure 9 and Figure 11. The power responses at first is increasing proportionally with the resistance load, but after reaching a certain point it is declining while the resistance increased. The resistance load that gives the maximum power response is the first resistance load before the voltage response goes asymptotic.

In a wider range of resistance loads, the voltage and power responses are plotted by logarithmic to logarithmic scale in Figure 18 and Figure 19 (the responses are not normalized to g such previously done for the base excitation model). In Figure 16 and Figure 17, the range of resistance loads used are between 0-10 Ω. The resistance loads at maximum power amplitude are around 1.88 Ω at 1Hz, 1.33 Ω at 2 Hz and 0.74 Ω at 3 Hz. Figure 18 shows the voltage responses become asymptotic even until the order of 10^3 Ω.

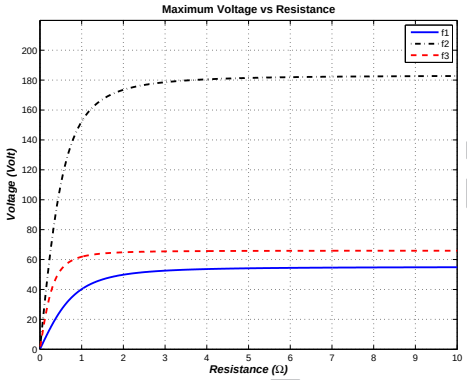

Figure 16: Wingbox voltage amplitude vs resistance

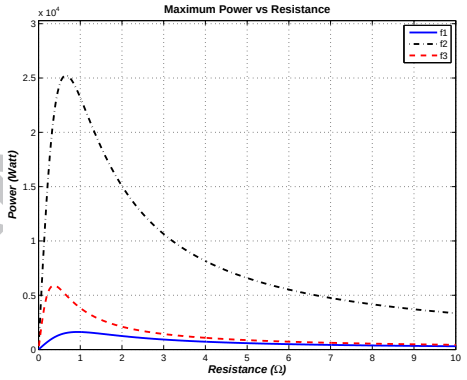

Figure 17: Wingbox power amplitude vs resistance

Figure 19 shows the optimum power is achieved in a small range of resistance loads, around 10^{-1} Ω to 10^1 Ω. Within this range, electrical power in order of 10^2 watts to 10^3 watts is achievable. However, the power is dropped significantly outside of this area. Therefore, the selection of the resistance loads is critical to design an optimum harvester configuration.

Moreover, a positive insight could be captured based on the results of this simulation. The power amplitude in the of order tens kilowatts is achievable (maximum 25.24 kW at 2 Hz excitation). This is considered a promising values, since the excitation given are also in the condition of cruise loads. If this amount of power could be sustained during a practical flight, it could becomes an alternative electrical power source for the aircraft, i.e. support for Auxiliary Power Unit.

7. Conclusion

A mathematical model and computational scheme to evaluate a cantilevered piezoelectric energy harvester under dynamic bending has been developed.

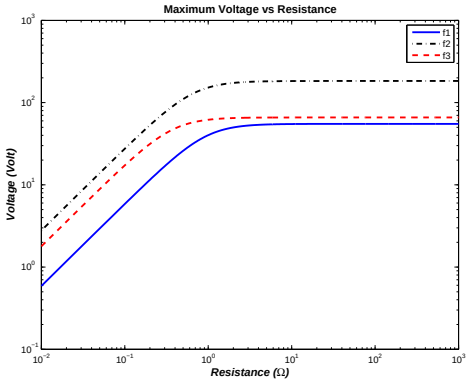

Figure 18: Wingbox voltage amplitude vs resistance, loglog scale

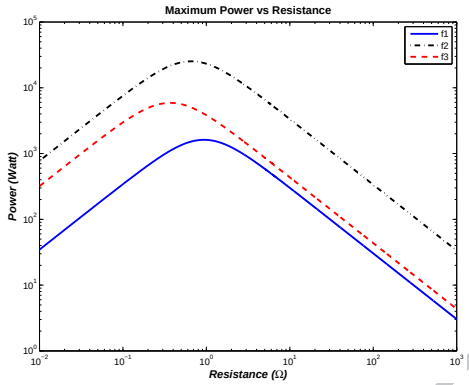

Figure 19: Wingbox power amplitude vs resistance, loglog scale

A semi-FEM computational scheme is applicable. Thus, various form of excitation problems and complex structural configurations are evaluable. The capabilities and robustness of the scheme is shown by comparison with results from the literature.

In this paper, a simulation for a notional civil jet aircraft wingbox with piezoelectric skin layer has been presented. Based on the simulation results, the voltage and power responses could attain a promising level, in the order of 10^1 to 10^2 volts and 10^2 to 10^4 watts.

However, there are still some issues to be addressed related to the aircraft design process. One of the major issue is the weight increment on the aircraft structure due to the existence of piezoelectric material. The commercially available piezoelectric materials are 3 times heavier than the common aluminium alloy used in the aircraft structure, i.e. Al-2219, Al-7075. This issue should be addressed in the design process to gain the optimum weight-power exchange.

Another issue yet to be observed is the strength of the composite with the piezoelectric layers, as these materials known to have brittle nature. It is worth adding that the investigations for piezoelectricity in polymers has also been conducted for several decades, such as one of the earliest reported work of Ueda and Carr [37], for the piezoelectricity in polyacrylonitrile (PAN). As PAN is also a well-known fiber used for aircraft′s composite materials, this is a promising insight for further evaluating the piezoelectric fiber on the aircraft composites.

Acknowledgements

The authors gratefully acknowledge Dr. Anton Krynkin for the fruitful discussions and the support of Indonesia Endowment Fund for Education (LPDP).

References

[1] Christodoulou L, Venables JD. Multifunctional material systems: The first generation. JOM 2003;55(12):39–45.
[2] Gibson RF. A review of recent research on mechanics of multifunctional composite materials and structures. Compos Struct 2010;92(12):2793 –810.
[3] Thomas JP, Qidwai MA, Kellogg JC. Energy scavenging for small-scale unmanned systems. J Power Sources 2006;159(2):1494 –509.
[4] Anton SR, Sodano HA. A review of power harvesting using piezoelectric materials (2003-2006). Smart Mater Struct 2007;16(3):R1.
[5] Selvan KV, Mohamed Ali MS. Micro-scale energy harvesting devices: Review of methodological performances in the last decade. Renew Sustain Energy Rev 2016;54:1035 –47.
[6] Thomas JP, Keennon M, DuPasquier A, Qidwai MA, Matic P. Multifunctional structure-battery materials for enhanced performance in small unmanned air vehicles. Proc ASME IMECE 2003;98:289–92.
[7] Thomas JP, Qidwai MA. The design and application of multifunctional structure-battery materials systems. JOM 2005;57(3):18–24.
[8] Anton SR, Inman DJ. Vibration energy harvesting for unmanned aerial vehicles. Proc SPIE Act Passiv Smart Struct Integr Syst 2008;6928:692824.
[9] Erturk A, Anton SR, Inman DJ. Piezoelectric energy harvesting from multifunctional wing spars for UAVs - Part 1: Coupled modeling and preliminary analysis. Proc SPIE Act Passiv Smart Struct Integr Syst 2009;7288:72880C.
[10] Anton SR, Erturk A, Inman DJ. Piezoelectric energy harvesting from multifunctional wing spars for UAVs - Part 2: Experiments and storage applications. Proc SPIE Act Passiv Smart Struct Integr Syst 2009;7288:72880D.
[11] Erturk A, Inman DJ. Issues in mathematical modeling of piezoelectric energy harvesters. Smart Mater Struct 2008;17(6):065016.
[12] Erturk A, Inman DJ. A distributed parameter electromechanical model for cantilevered piezoelectric energy harvesters. J Vib Acoust 2008;130(4):041002.

[13] Erturk A, Inman DJ. An experimentally validated bimorph cantilever model for piezoelectric energy harvesting from base excitations. Smart Mater Struct 2009;18(2):025009.
[14] Erturk A, Vieira WGR, De Marqui Jr. C, Inman DJ. On the energy harvesting potential of piezoaeroelastic systems. Appl Phys Lett 2010;96(18):184103.
[15] De Marqui Jr. C, Erturk A, Inman DJ. Piezoaeroelastic modeling and analysis of a generator wing with continuous and segmented electrodes. J Intell Mater Syst Struct 2010;21(10):983–93.
[16] De Marqui Jr. C, Vieira WGR, Erturk A, Inman DJ. Modeling and analysis of piezoelectric energy harvesting from aeroelastic vibrations using the doublet-lattice method. J Vib Acoust 2011;133(1):011003.
[17] De Marqui Jr. C, Erturk A. Electroaeroelastic analysis of airfoil-based wind energy harvesting using piezoelectric transduction and electromagnetic induction. J Intell Mater Syst Struct 2013;24(7):846–54.
[18] Dias JAC, De Marqui Jr. C, Erturk A. Three-degree-of-freedom hybrid piezoelectric-inductive aeroelastic energy harvester exploiting a control surface. AIAA J 2015;53(2):394–404.
[19] Amini Y, Emdad H, Farid M. Finite element modeling of functionally graded piezoelectric harvesters. Compos Struct 2015;129:165–76.
[20] Amini Y, Fatehi P, Heshmati M, Parandvar H. Time domain and frequency domain analysis of functionally graded piezoelectric harvesters subjected to random vibration: Finite element modeling. Compos Struct 2016;136:384–93.
[21] Abdelkefi A. Aeroelastic energy harvesting: A review. Int J Eng Sci 2016;100:112–35.
[22] Xiang J, Wu Y, Li D. Energy harvesting from the discrete gust response of a piezoaeroelastic wing: Modeling and performance evaluation. J Sound Vib 2015;343:176–93.
[23] Lenk A, Ballas RG, Werthschützky R, Pfeifer G. Electromechanical Systems in Microtechnology and Mechatronics: Electrical, Mechanical and Acoustic Networks, their Interactions and Applications; chap. 9. Microtechnology and MEMS; Springer Berlin Heidelberg. ISBN 9783642108068; 2010, p. 313–412.
[24] Standards Committee of the IEEE Ultrasonics, Ferroelectrics, and Frequency Control Society . IEEE Standard on Piezoelectricity. ANSI/IEEE Std 176-1987 1988;.
[25] Ballas RG. Piezoelectric Multilayer Beam Bending Actuators: Static and Dynamic Behavior and Aspects of Sensor Integration; chap. 6. Microtechnology and MEMS; Springer Berlin Heidelberg. ISBN 9783540326427; 2007, p. 103–22.
[26] Ballas RG. Piezoelectric Multilayer Beam Bending Actuators: Static and Dynamic Behavior and Aspects of Sensor Integration; chap. 4. Microtechnology and MEMS; Springer Berlin Heidelberg; 2007, p. 48–76.
[27] Ballas RG. Piezoelectric Multilayer Beam Bending Actuators: Static and Dynamic Behavior and Aspects of Sensor Integration; chap. 9. Microtechnology and MEMS; Springer Berlin Heidelberg. ISBN 9783540326427; 2007, p. 173–96.
[28] Erturk A, Inman DJ. Piezoelectric Energy Harvesting; chap. 5. John Wiley & Sons; 2011, p. 131–50.
[29] Lu F, Lee H, Lim S. Modeling and analysis of micro piezoelectric power generators for micro-electromechanical-systems applications. Smart Mater Struct 2004;13(1):57–63.
[30] Beeby S, Tudor M, White N. Energy harvesting vibration sources for microsystems applications. Meas Sci Technol 2006;17(12):R175–95.
[31] Erturk A, Inman DJ. Piezoelectric Energy Harvesting; chap. 3. John Wiley & Sons; 2011, p. 49–96.
[32] Erturk A, Inman DJ. Piezoelectric Energy Harvesting; chap. 4. John Wiley & Sons; 2011, p. 97–130.
[33] Ainsworth J, Collier C, Yarrington P, Lucking R, Locke J. Airframe wingbox preliminary design and weight prediction. In: 69th Annual Conference on Mass Properties, Virginia Beach, Virginia. 2010, p. 41.
[34] Curiel Sosa JL, Gil A. Analysis of a continuum-based beam element in the framework of explicit-FEM. Finite Elem Anal Des 2009;45(89):583 –91.
[35] Curiel Sosa JL, Beg OA, Liebana Murillo JM. Finite element analysis of structural instability using an implicit/explicit switching technique. Int J Comput Methods Eng Sci Mech 2013;14(5):452–64.
[36] MSC Software Corporation . MSC Nastran 2014 Dynamic Analysis User's Guide; chap. 4. Springer Berlin Heidelberg; 2014, p. 133–65.
[37] Ueda H, Carr S. Piezoelectricity in polyacrylonitrile. Polymer 1984;16(9):661–7.